An experimental study of the thermal-hydraulics of a spent nuclear fuel pool under loss-of-cooling accident conditions. Part I: The MIDI facility and its main experimental results

Benoît Migot, Jimmy Martin

An experimental study of the thermal-hydraulics of a spent nuclear fuel pool under loss-of-cooling accident conditions

Part I: the MIDI facility and its main experimental results

B. Migot* and J. Martin

Institut de Radioprotection et de Sûreté Nucléaire, PSN-RES, CEN Cadarache, BP3, 13115, Saint-Paul-lez-Durance, France

*Corresponding author: benoit.migot@irsn.fr

Abstract

Motivated by the 2011 accident at the Fukushima Daiichi nuclear power station, the French Institute for Radiation Protection and Nuclear Safety (IRSN) launched in 2014 the DENOPI project. This research program, supported by the French Government and carried out in collaboration with national and international partners, dealt with the open issues of spent fuel pool accidents. As part of this project, a test facility named MIDI was designed and built at the IRSN's research unit of Cadarache, France. The MIDI facility is an experimental tool which aims at reproducing the thermal-hydraulic phenomena that may occur at an integral scale in a spent fuel pool undergoing a loss-of-cooling accident, before the stored fuels get uncovered. This paper first describes the MIDI facility and its instrumentation and the test matrix achieved to date. An overview of its main results is then provided. In the framework of the DENOPI project, nine tests were achieved and allowed investigating the phenomenology of this type of accident. The highlighted phenomenology is characterized by three competing liquid vaporization modes: the evaporation at the pool free surface, the nucleate boiling within the fuel bundles and the gravity-driven flashing of superheated water on top of the storage racks. The existence of the latter vaporization mode, uncertain at the launch of the DENOPI project, is now confirmed in the configuration of a spent fuel pool.

Keywords

Gravity-driven flashing, superheated water, free surface evaporation, pool boiling, integral scale experiment.

1. INTRODUCTION

During the Fukushima Daiichi nuclear power plant accident that occurred in March 2011, the station's reactor unit 4 was in a refueling stage and its spent fuel pool (SFP), referred to as SFP-4, contained the largest powered fuel assembly inventory, with an overall initial decay heat that summed up to 2.28 MW. When the SFP-4 cooling system was shut down following a loss-of-offsite power, the liquid pool temperature increased up to 90°C and the water level almost dropped down to the so-called top-of-active-fuel location, as reported by the licensee, *Tokyo Electric Power Company* [1]. The accident was finally mitigated by means of significant water injections, thereby preventing the uncovery of the stored fuels. Despite this fortunate outcome, the event clearly renewed interests in SFP safety issues within the community. As a manifestation of these interests, a phenomena identification ranking activity related to SFP accidents was conducted at the *Nuclear Energy Agency* of the *Organization for Economic Cooperation and Development* [2]. From this analytical work, it appeared that the validation database of most computer codes currently utilized for SFP deterministic safety

analyses (system codes, severe accident codes) needed to be extended to SFP configurations [3]. Indeed, on one hand, the thermal-hydraulics of a SFP is mainly based on three-dimensional natural convection two-phase heat and mass transfers, at a pressure around one atmosphere and with a relatively low heat load, what clearly differs from in-reactor conditions [1]. On the other hand, these computation codes had not been primarily developed for the specific purpose of SFP simulations [1]. Moreover, as admitted by the community, some knowledge gaps regarding SFP accident phenomenology emerged and needed to be addressed by means of novel experiments [2], [3].

In this context, the French *Institute for Radiation Protection and Nuclear Safety* (IRSN) launched in 2014 the so-called DENOPI project, a research program which included both experimental and modeling activities. As part of this project, a test facility named MIDI was designed and constructed at IRSN, within the Cadarache nuclear research center (France). This facility, reproducing at the laboratory scale the integral characteristics of a prototypical French SFP, was specifically developed for addressing the issues, highlighted in [2], relating to a spent fuel pool loss-of-cooling accident before the nuclear fuels get uncovered by water. Among those issues was the quantification of each vaporization process that may come into play in the course of such accident, under some given set of initial and boundary conditions. Indeed, three vaporization modes were early recognized as being potentially competing during a spent fuel pool loss-of-cooling transient: the *free surface evaporation*, the *nucleate boiling of water* along the spent fuels and the *gravity-driven flashing of superheated water* [2]. If bubbles were to nucleate in the course of an accident, this would in turn prevent any restarting of the SFP cooling system and would contribute to the release of various radionuclides that can be classically met within the SFP water, well before the spent nuclear fuels get uncovered [1], thereby justifying the need to better understand and quantify the occurrence conditions of each envisioned vaporization mode. Furthermore, at the start of the DENOPI project, the gravity-driven flashing of superheated water was judged hypothetical in the specific configuration of a pool and the existence of any possible liquid superheat still debated [4]. At the time, it was first assumed that, if existing, the flashing would take place preferentially onto any immersed solid and rough surface, as suggested in [5]. The pre-existence of enough gas *nuclei* (*i.e.* some freely-floating tiny bubbles) within the liquid bulk for initiating this vaporization mode had also to be investigated [5]. At last, the prediction of the natural convection flow that is expected to develop at pool scale was still considered as an open issue in the general case of a heterogeneous spent fuels loading pattern within the SFP by the community [2]. The topic, judged as important with regards to the SFP safety [6], included the understanding of the two-phase instabilities that may potentially arise from a heterogeneous spent fuels loading, when no crossflows are practically possible within the storage racks [7].

In this article, the MIDI facility is first described (Section 2) and its instrumentation introduced (Section 3). Next are presented the test matrix achieved to date in the frame of the DENOPI project (Section 4) and the conducted test procedure (Section 5). At last, the obtained empirical results are provided and widely discussed (Section 6). In addition, the interested reader may note that a first physical interpretation of the MIDI tests that were conducted up to date is provided in the second part of the present article, available in [8]. This interpretation includes a first-level phenomenological analysis, the quantification of the envisioned modes of water vaporization, the construction of a so-called vaporization regimes map which allows predicting the most likely dominant vaporization mode, given the pool level and total heat power, and a set of dimensionless correlations for estimating the heat and mass transfers within the liquid pool.

2. DESCRIPTION OF THE MIDI FACILITY

First of all, MIDI was scaled on the basis of the typical French SFP dimensions and maximum stored residual power given in Table 1. A geometrical scaling factor of 1:6 was initially chosen for complying with the economical and practical constraints inherent to the DENOPI project. Next, the height and total heating power of the facility were both distorted to allow studying in a parametric way the contribution of the three expected water vaporization modes, introduced earlier, to the pool energy budget: the free surface evaporation, the nucleate boiling of water along the spent fuels and the gravity-driven flashing of superheated water. The maximum scaling factor of the pool height was fixed to 1:3 and the maximum heating power to 300 kW. The last step was to check that the hydrodynamic and thermal regimes which might be reached during a SFP loss-of-cooling accident can be well reproduced at MIDI facility scale. For that purpose, a set of selected dimensionless numbers resulting from a similarity analysis introduced in [9], was computed for both MIDI and the prototypical SFP scales. Among those important quantities is the so-called *Rayleigh* number, which characterizes in a dimensionless way the intensity of the natural convection heat transfer within the liquid pool [10]. This number, which depends on the cubic power of the pool height, is expected to be of the order of 10^{13}-10^{15} in a prototypical SFP [4]. Those values clearly correspond to a turbulent regime of natural convection heat transfer [11]. By reducing the pool height by one order of magnitude with regards to a real SFP, as envisioned at MIDI scale (*cf.* Table 1), the Rayleigh number is then expected to differ by a factor 1/1000 and to stand in between 10^{10}-10^{12}, i.e. far above the threshold value of 10^5 separating the laminar and turbulent regimes of natural convection in water [11]. Next is the so-called *Jakob* number, which is seen in the present study as a dimensionless form of the maximum liquid superheat that may be reached in a SFP without boiling onto the heat source [9]. This maximum superheat which depends primarily on pool height, as justified in [9], is estimated to 20°C in a real SFP [4]. The chosen pool height distortion reduces this maximum superheat down to 6.5°C, a value which was however judged sufficient for allowing the gravity-driven flashing to develop within the MIDI facility. All in all, this definition stage led to the MIDI's dimensions and parameters listed in Table 1.

Parameters	MIDI facility	Prototypical SFP	Scale ratio
Maximum water level (m)	4.0	12.0	1/3
Bundle active length (m)	0.7	~ 4.0	~ 1/3
Basin width (m)	1.35	8.50	1/6
Basin length (m)	2.10	12.60	1/6
Rack flow section (m^2)	0.65	22.86	~ 1/35
Free surface area (m^2)	2.835	107.1	~ 1/36
Bundle width (m)	0.225	0.225	1/1
Bundle porosity (-)	0.61	0.57	~ 1/1
Number of cells (-)	21 (7X3)	792	~ 1/37
Power range (kW)	[50;300]	10 000	-
Max. power per bundle (kW)	50	58	~ 6/7
Volumetric power (kW/m^3)	[4.2;25.1]	7.8	-

Table 1 - Geometrical parameters of the MIDI facility and scaling factors.

An illustration of the resulting MIDI basin is given in Figure 1. The heat source in the lower part of the basin consists in 21 individual heating elements, representing 21 cells of a storage rack. Each heating element comprises an electrically heated rod bundle, organized as a 3x3 network of heated rods. The characteristics of the heating rods that constitute the bundle are:

- Rod maximum power: 5.6 kW, in agreement with a limiting maximum power per bundle of 50 kW;
- Rod active length: 0.67 m;
- Rod external diameter: 53 mm.

The heating elements are set up through the form of a regular arrangement of 7 x 3 cells in a single rack. No flows are allowed between the cells (*i.e.* the rack is made of solid walls). Hence, the cells may be seen as independent hydraulic channels. Moreover, the heated cell power can be individually controlled, thereby allowing studying the influence of the loading pattern of the spent fuels on the SFP thermal-hydraulics. On top of the pool, a ventilation hood continuously extracts the produced steam outside the experimental building.

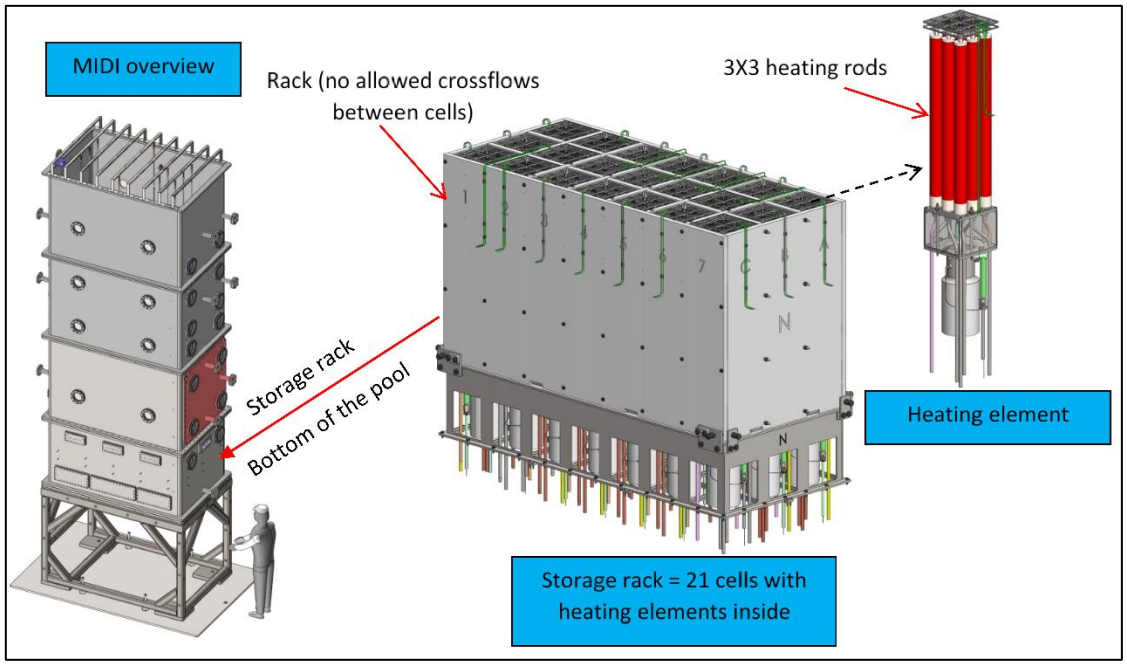

Figure 1: Illustration of the MIDI mock-up.

A 3D view of the MIDI facility is given in Figure 2. Two buffer containers of 7.5 m^3 each are located next to the MIDI basin. Connected to each other, they have an overall volume capacity of 15 m^3 which is greater than the volume of the MIDI basin (*cf.* Table 1). The filling of the MIDI basin is achieved prior to any test from the buffer tanks by means of a centrifugal pump. The drainage of the MIDI basin is done by gravity since the bottom of the basin is located above the top of the two buffer tanks. In addition, the facility includes an electric heater of 150 kW which allows a thermal pre-conditioning of the water that is to be utilized during a test. The MIDI basin is also equipped with several pipes arranged at different locations between the bottom and the top of the parallelepiped basin and connected to the circulation pump. These connections allow creating recirculation in the pool during the thermal conditioning stage. At last, the external lateral surfaces of the MIDI basin are all insulated by means of two layers of 32 mm of a synthetic foam with a low thermal conductivity (< 0.045 W/m/K).

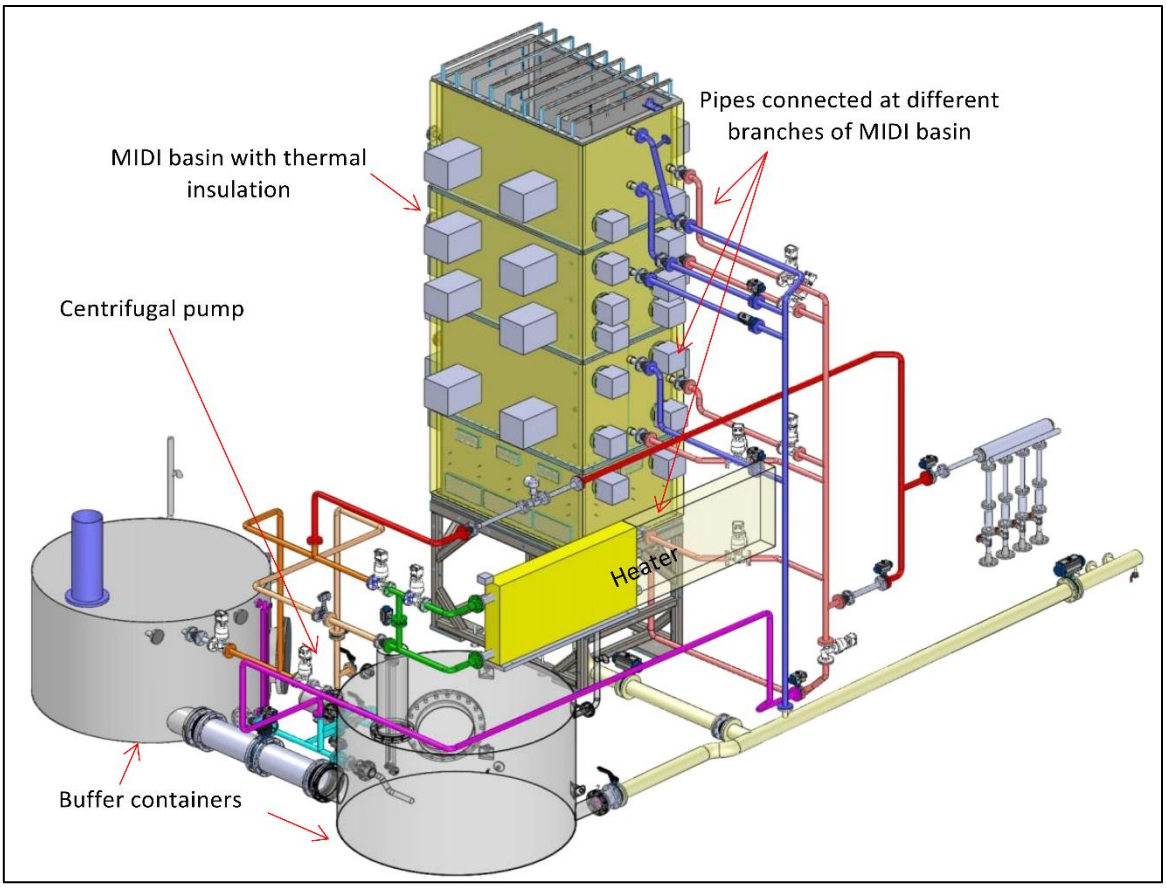

Figure 2: 3D view of the MIDI facility.

3. INSTRUMENTATION OF THE MIDI FACILITY

To study the natural convection flows and vaporization regimes introduced above, some key thermal-hydraulic measurements are continuously achieved within each heated cell, within the pool and at MIDI's boundaries. First, the determination of the enthalpy flowrates at the inlet and outlet of each cell is carried out thanks to:

- Fluid temperature measurements at the inlet and the outlet of the latter, using class 1 T-type thermocouples with a 1-mm diameter sheath;
- Overall inlet mass flow rate measurements using a vane wheel flow sensor (a specific calibration was performed to convert the velocity information given by the sensor as a mass flow rate);
- Heating power determination by recording the voltage and current intensity of each heating rod;
- The determination of the area-averaged void fraction at each outlet cell, indirectly, in a dedicated hydraulic loop, as a prior stage. This loop (see Figure 3) allowed obtaining the expected values of the void fraction at the outlet of a typical heated cell as a function of the inlet enthalpy flowrate, heating power and absolute pressure, by means of a so-called Wire-Mesh-Sensor [12].

Next, some key measurements are performed within the pool for characterizing the heat and mass transfers taking place at that very location:

- The measurement of the pool water level using a pressure gauge, for determining a collapsed level and a guided level–radar probe, for obtaining a swelled level;

- The measurement of local temperatures within the liquid upper volume using 9 Pt-100 multipoint sensors and comprising each, 7 class A Pt-100 probes of a 1.5-mm shealth diameter, separated from each other by 0.5 m;
- The measurement of the free surface temperature by means of a network of pyrometers;
- The direct visualization of the liquid pool through optical windows, with standard cameras at a recording rate of 25 frames per second.

The positions of the multipoint temperature sensors and pyrometers that were set up for the tests described in the present paper are shown in Figure 4.

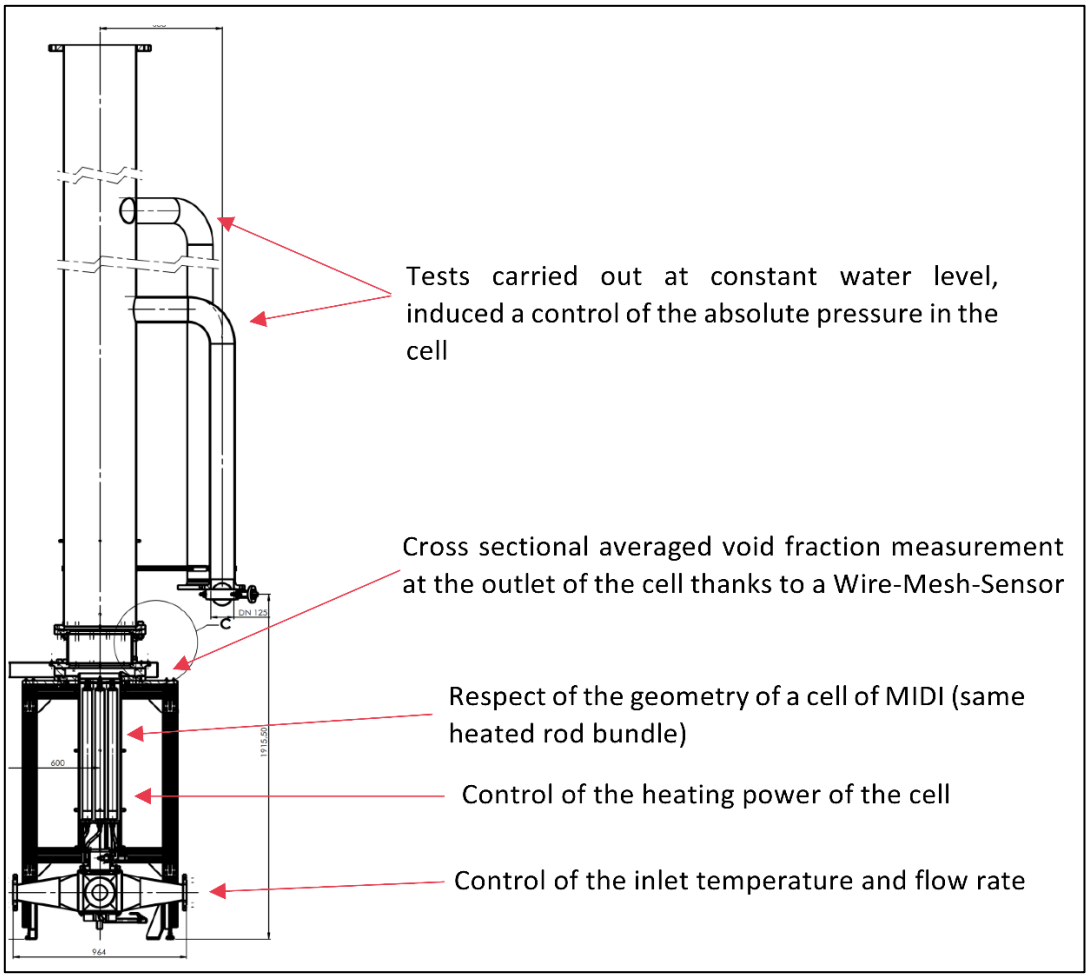

Figure 3: Illustration of the specific loop which was built to characterize the void fraction expected at the outlet of each heated cell.

Pool boundary conditions are monitored as well. In details, the gas temperature, total pressure, and relative humidity of the atmospheric volume above the pool free surface are all measured with one multi-parameter probe. Moreover, the temperatures of the external walls of the pool are measured too, to estimate the magnitude of the thermal losses throughout any test. For doing so, around 80 class 1 T-type thermocouples are distributed onto those external walls and separated from each other by a distance between 0.5 m and 1 m. In addition, the quality of the utilized demineralized water is continuously monitored using an electric conductivity probe and a dissolved oxygen sensor.

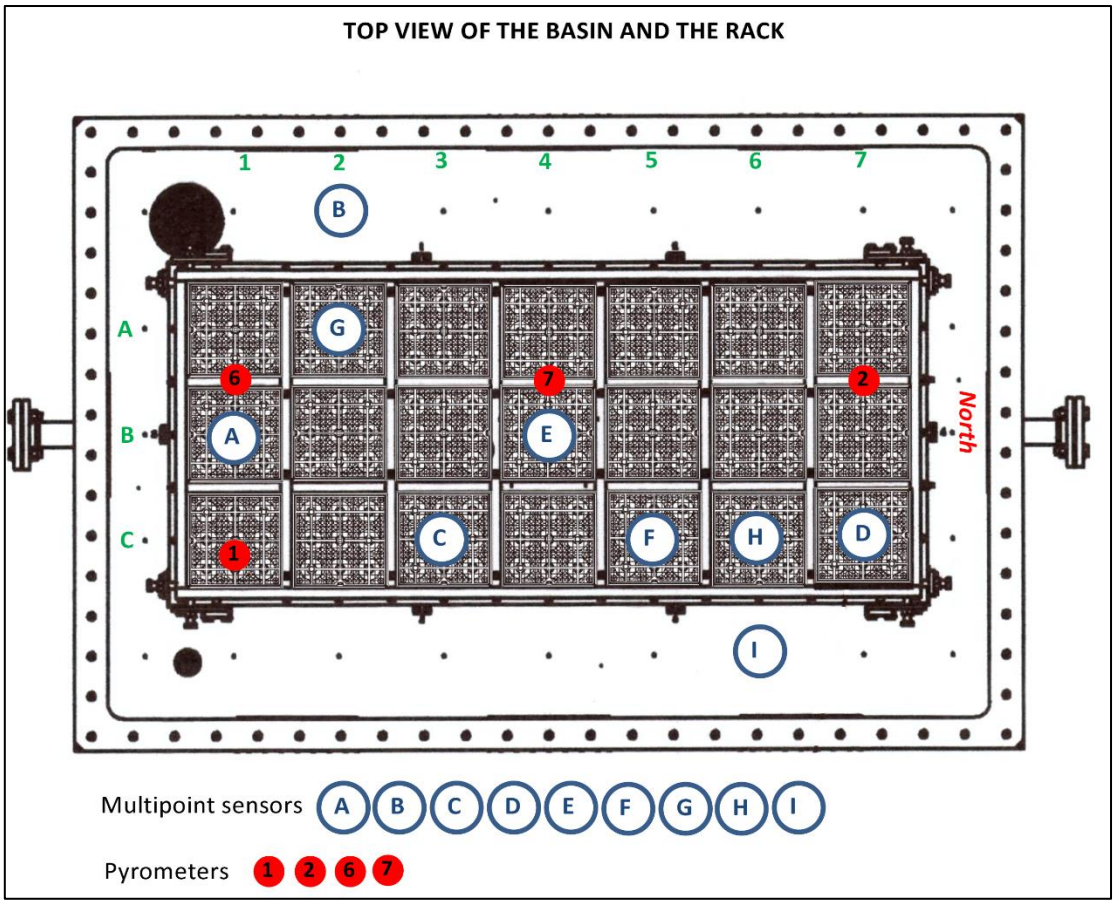

Figure 4: Position of the utilized multipoint sensors and pyrometers.

At last, Table 2 summarizes the range and the associated uncertainty of the main physical parameters that are measured within the MIDI facility.

Variable type	Range	Standard or relative uncertainty
Temperature from T-type thermocouple	-40°C to 125°C	+/- 0.9 °C
Temperature from Pt-100 probes	15°C to 110°C	+/- 0.2 °C at 15°C +/- 0.5 °C at 110°C
Temperature from pyrometer	15°C to 150°C	+/- 1.9 °C
Flowrates in the cells	-12 kg/s to 12 kg/s	+/- 5 % for -12 kg/s to -0.5 kg/s +/- 7.5 % for 0.5 kg/s to 12 kg/s
Water level from pressure gauge	0 to 5000 mm	+/- 0.2 %
Water level from guided level-radar probe	1340 to 4670 mm	+/- 3 mm
Gas temperature above the free surface	15°C to 110°C	+/- 0.1 °C
Relative humidity above the free surface	0 to 100 %	+/- 1%
Atmospheric pressure	500 to 1100 hPa	+/- 0.1 hPa
Water conductivity	0.01 to 200 µS/cm	+/- 2%
Dissolved oxygen concentration in water	0 to 15 mg/L	+/- 2%
Void fraction from the Wire-Mesh-Sensor	0 to 100 %	+/- 15 % [12]

Table 2 – Main instrumentation of MIDI facility and its associated uncertainties.

All uncertainties shown in Table 2, excluding the one in link with the void fraction, include sensor and acquisition chain tolerances, as well as a coverage factor of 2. In turn, the uncertainty associated with the heated cells outlet void fraction measurement is estimated from [12], which discusses the precision of Wire-Mesh-Sensor-based void fraction measurements.

4. CONTROL PARAMETERS AND TESTS MATRIX

Three control parameters were considered during the tests performed to date. The first two are the overall heating power and the initial pool level, which were varied within the following ranges:

- Heating power: 50 kW – 300 kW;
- Initial pool level: 2 m – 4 m.

Another key parameter is the heating power distribution within the simulated storage rack, later referred to as "loading pattern". Four loading patterns were chosen for this first experimental campaign. Those patterns are summarized in Table 3 and are all illustrated in Figure 5 (the visible red tones indicate the magnitude of the simulated heating power: higher values are darker, lower values are lighter). The first loading pattern, denoted as LP1, is a uniform power distribution within the storage rack whereas the second one, referred to as LP2, is a regular pattern of "hot" and "cold" heat sources. The heating power ratio between the "hot" and "cold" heat sources was defined with the aim to mimic a SFP configuration that can be met during a French 900 MWe pressurized-water-reactor refueling stage. The third configuration, referred to as "hot spot" or LP3, simulates a specific case where all the recently discharged spent fuels would be stored in a concentrated way. It can be considered as the most conservative pattern regarding spent fuels coolability [13]. Hence, it was chosen to investigate it within the MIDI facility. At last is the so-called "irregular" loading pattern, denoted as LP4.

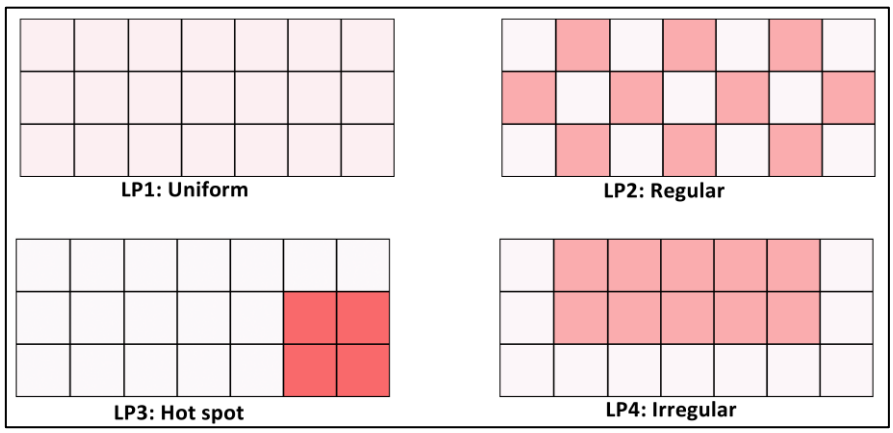

Figure 5: The heat source loading patterns tested in MIDI facility during the DENOPI program.

Reference	Type of loading pattern	"Hot cells"	"Cold cells"
LP1	Uniform	21 (100 % overall power)	-
LP2	Regular	10 (91 % overall power)	11 (9 % overall power)
LP3	Hot spot	4 (91 % overall power) or 4 (66 % overall power)	17 (9 % overall power) or 17 (34 % overall power)
LP4	Irregular	10 (91 % overall power)	11 (9 % overall power)

Table 3 – Types of loading patterns. Within the "hot cells" and "cold cells" columns is first indicated the number of involved cells. Then is given their total heating power as a percentage of the overall power.

One may note that for the tests discussed in the present article, no additional flow restriction device was placed neither at the inlet nor at the outlet sections of the heated cells, although it is technically achievable. This possibility was left as a perspective of the present work. Regarding the utilized coolant, all tests were carried out with demineralized water. The electric conductivity and dissolved oxygen content of the latter fluid were both measured at the beginning of each test. No severe criterion on water conductivity was imposed: it was just checked that the value was kept below approximately 25 µS/cm at the start of the simulated transient. For the oxygen concentration, an initial target value around 6 mg/L was chosen. This value corresponds to the oxygen solubility limit of water at a temperature around 50°C, which is the temperature at which each test was initiated. At last is given the MIDI tests matrix which was achieved in the frame of the DENOPI project (*cf.* Table 4). As one can notice, the matrix comprises nine different tests. Five of those tests were conducted twice, for assessing their repeatability. The first four tests were intended to assess the influence of the loading pattern on the flow topology and vaporization regimes and were all conducted at a total heating power of 93 kW. The next two tests, carried out at a power of 300 kW and the other test conducted at a power 220 kW helped evaluating the impact of the overall heating power on the occurrence of the three envisioned vaporization regimes. In addition, to assess the influence of the initial pool level, a test was carried out at 300 kW, but with an initial pool level of 2 m instead of the standard value of 4 m. Finally, the last of those tests was performed under low heating power conditions, with the aim to promote the dominance of the free surface evaporation in the liquid pool energy budget, corresponding to the energetic configuration of the Fukushima-Daiichi SFP-4 during the March 2011 nuclear accident [1]. In this very case, the free surface evaporation was most likely the dominant vaporization mode, owing to the measured SFP-4 liquid temperatures which remained below 90°C [14].

Test	Number of runs	Overall heating power (kW)	Initial pool level (m)	Loading pattern	Number of hot cells / Heating power in hot cells (kW)	Number of cold cells / Heating power in cold cells (kW)
1	2	93	4	LP1	21 / 4.4 (kW)	0 / 0 (kW)
2	2	93	4	LP2	10 / 8.5 (kW)	11 / 0.8 (kW)
3	1	93	4	LP3	4 / 21.2 (kW)	17 / 0.5 (kW)
4	2	93	4	LP4	10 / 8.5 (kW)	11 / 0.8 (kW)
5	2	300	4	LP2	10 / 27.3 (kW)	11 / 2.5 (kW)
6	1	300	4	LP3	4 / 49.5 (kW)	17 / 6.0 (kW)
7	1	300	2	LP2	10 / 27.3 (kW)	11 / 2.5 (kW)
8	1	220	4	LP3	4 / 50.0 (kW)	17 / 1.2 (kW)
9	2	55	4	LP3	4 / 11.4 (kW)	17 / 0.6 (kW)

Table 4 – The MIDI tests matrix.

5. TEST PROCEDURE

The test procedure which was applied to each test discussed in the present article consisted in the three following stages:

1. Filling stage: the basin is first filled-up until the required level is reached. Appropriate precautions to obtain demineralized water with 6 mg/L of oxygen dissolved oxygen at 50°C are taken.

2. Thermal conditioning stage: water is heated up to 50°C ± 1.5 °C using the pool heating elements, by forced convection, thereby leading to a homogeneous temperature field within the pool and without any stratification. During this stage, when the system is maintained at 50°C, the power regulation system equipping the facility allows determining the thermal losses at the basin's boundaries, at a reference temperature of 50°C.

3. Experimental stage: once the facility pre-conditioning is achieved, the forced convection is stopped, the basin is isolated by closing all the valves of the auxiliary loops and the test starts by imposing to the pool a pre-selected overall heating power and a given loading pattern. Then the pool heats up and its liquid vaporizes gradually. The test stops when the remaining pool collapsed level reaches +60/50 cm above the top of the rack.

6. EXPERIMENTAL RESULTS

In what follows, the experimental results obtained for each test of the matrix given in Table 4 are discussed. An overall phenomenological picture of those tests is first depicted in Section 6.1. Then are successively discussed in the following sections the observed time-trends of the vaporization rate, the liquid superheating degree, the fluid temperatures, the mass flowrates in the heated cells and the amount of dissolved oxygen within the liquid.

6.1 The typical phenomenology of a test

First of all, Figure 6, shows the time-trends of the water mass (green plot) and volume-averaged liquid pool temperature (blue plot) throughout a 300kW test conducted with a regular loading pattern. Those trends are typical to any test and are therefore worth being described. Initially, a linear increase of the liquid pool temperature from 50°C to 100°C is systematically observed. Concomitantly, the liquid mass starts decreasing because of the free surface evaporation. In the meantime, the liquid supersaturates in dissolved gases. Indeed, the dissolved gases solubility is a decreasing function of the liquid temperature. As a way to tend toward a chemical equilibrium between the dissolved air and the gaseous one underneath the liquid free surface, a degassing process spontaneously occurs, through the form of a mix between pure diffusion and an air bubbles nucleation process, which intensifies as the temperatures get closer to thermal saturation. Once this very condition is reached, the pool temperature roughly stabilizes around 100°C, while at the same time the water mass starts decreasing steadily.

It is during this stage of the test that the three envisioned vaporization modes (evaporation at free surface, gravity-driven flashing of superheated water, nucleate boiling onto the fuel assemblies) can coexist and be more or less dominant, depending on the instant water level, of the imposed type of loading pattern and of the total heating power. At the beginning of the thermal saturation plateau visible in Figure 6, while the water level is high enough, many steam bubbles are spontaneously produced by gravity-driven flashing, underneath the free surface (see Figure 7,a), in agreement with a prior observation of the phenomenon in a pool-type geometry, reported in [4], [9]. It is worth noting that during any MIDI test, the gravity-driven flashing is characterized by a sudden and intermittent production of steam bubbles, as observed in genuine *geysers* [15], but contrarily to what was evidenced in [4], [9]. This difference between those two evidences of the phenomenon is understood as being due to the particular geometry of MIDI's heat source, which promotes the formation of hot plumes at the outlet section of the heated cells. In turn, the experiment described in [4], [9] is based on a simplified, planar heat source. Those plumes of hot water, when flowing upwardly, are assumed to reach a superheating state because of the decrease of hydrostatic pressure oriented toward the free surface. If one of those plumes reaches a zone of the pool with enough gas *nuclei*, its superheated liquid may spontaneously relax toward thermal saturation by vaporizing (this is namely the flashing process). But this process is expected to locally cool down the liquid, by latent heat removal. Some delay is hence necessary for regenerating at that very location the thermodynamic conditions promoting the flashing process, which might explain the observed intermittent behavior of this vaporization mode. In addition, during the conducted tests, the flashing phenomenon lasts long after the liquid has been completely degassed, which clearly questions the origin of the gas *nuclei* behind the spontaneous production of bubbles. Obviously, this vaporization mode widely disturbs the liquid free surface, with an intensity that gets higher as the heating power is increased. Typically, for the tests conducted with a heating power upper than 200 kW, when the flashing bubbles burst at the free surface, they induce spectacular projections and spurts of water that are very similar to the ones of genuine *geysers*. Pointedly, for the "hot spot" loading pattern, it is observed that the vapor bubbles created by flashing are preferentially located above the cells where most of the heating power is concentrated. Further on, as the water level decreases, vapor bubbles gradually appear at the outlet of the hot cells where the heating power is at its highest value (see Figure 7, b). For that vaporization mode, bubbles are obviously created onto the hot walls of the heated rods, but initially recondense as soon as they leave the rack, since the hot plume into which those bubbles are flowing is mixed with the cooler liquid of the pool upper volume. Eventually, those bubbles reach the liquid free surface and contribute to the liquid loss of mass, only lately during the conducted tests, when the water volume covers the heated rack by about one meter. Hence, the lower the water level, the higher the contribution of the nucleate boiling to the overall vaporization, with the gravity-driven flashing contribution evolving in the opposite way. Ultimately, as visible in Figure 6, as soon as the heating power is set to zero, the

pool temperature and water mass both start decreasing, because the liquid remains hot enough for a while and thus continues to evaporate through its free surface.

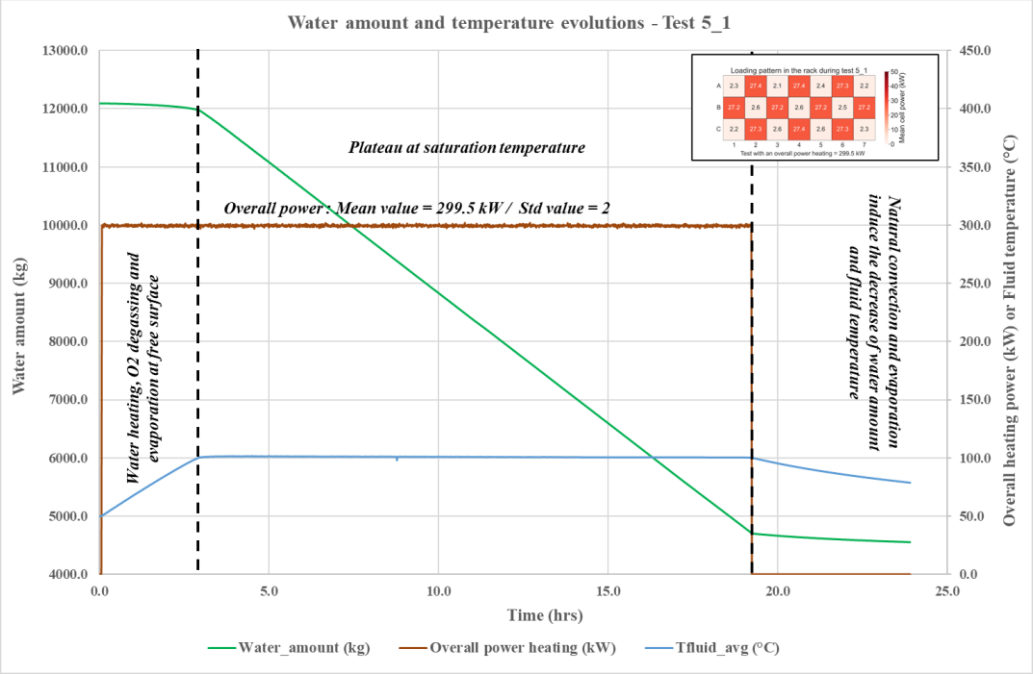

Figure 6: Time-trends of the water mass (green plot) and of the volume-averaged liquid pool temperature (blue plot) during a test achieved at a heating power of 300 kW.

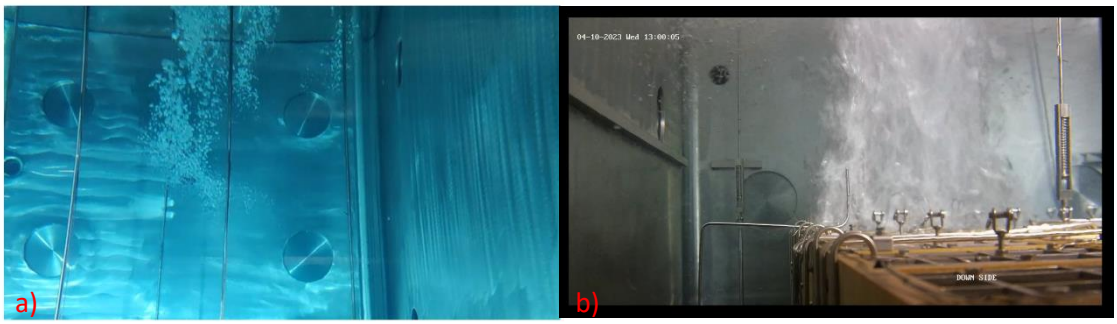

Figure 7: Vapor bubbles produced by gravity-driven flashing of superheated water (a). Vapor bubbles generated by nucleate boiling (b).

6.2 Vaporization rates

The total vaporization rate is estimated by means of the computation of the numerical derivative of the measured water mass for each conducted test. Figure 8 gives the time-trends of the vaporization rates computed that way. As one can observe, the vaporization rate tends to increase toward a stabilized value which is reached

when the liquid temperature stabilizes around its thermal saturation value. This constant value only depends on the total heating power.

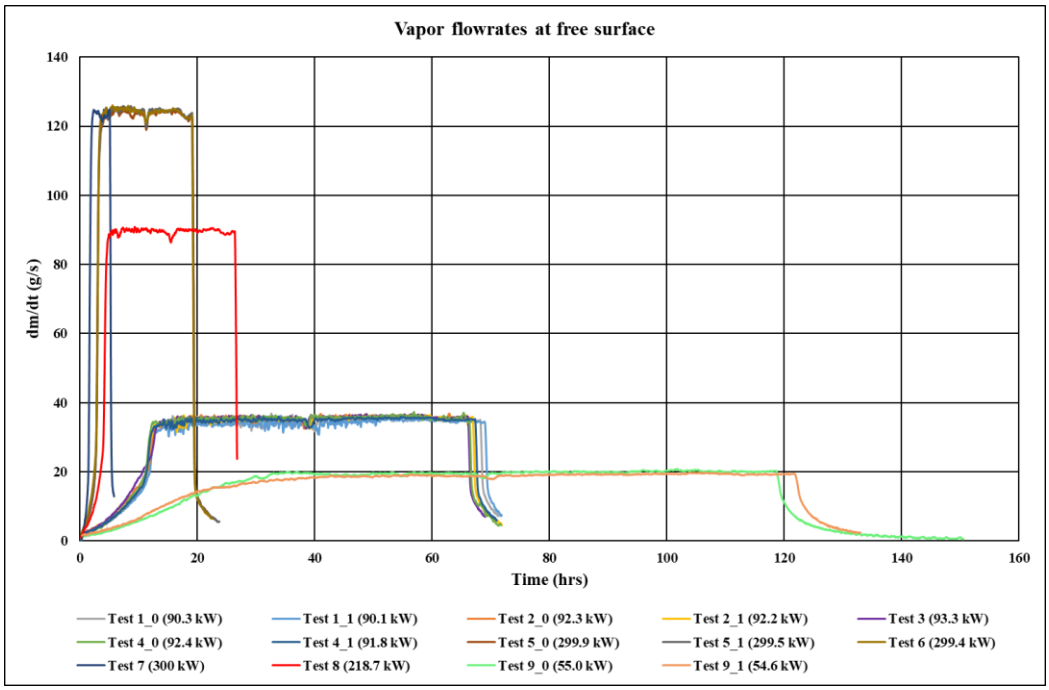

Figure 8: The time-trends of the vaporization rate of each test.

In Table 5, the time-averaged steady vaporization rates of each test is given. During this very stage, the liquid pool energy balance can be written as follows:

$$P_{heating} \approx \frac{dm}{dt} h_{fg} + P_{losses}$$

with $P_{heating}$ the overall heat power, dm/dt the vaporization rate, h_{fg} the latent heat of, P_{losses} the thermal losses through the walls of the basin. The latter are estimated from the thermal measurements performed onto the side walls (*cf.* Section 3), from the measured ambient temperature and from an estimated value of 10 W/m²/K for the natural convection coefficient characterizing the heat losses at pool's boundaries. The computation of all of the above quantities allows assessing the adequacy of the performed measurements with regards to the estimate of the pool energy balance. As one can notice from Table 5, the pool's energy balance is well verified on that basis, thereby confirming the reliability of the performed measurements.

Test ref.	$P_{heating}$ (kW)	Vapor flowrate (g/s)	Vaporization power (kW)	P_{losses} (kW)	Energy balance (%)
1_0	90.3	34.6	78.2	9.5	-2.9
1_1	90.1	34.2	77.3	10.8	-2.2
2_0	92.3	35.6	80.4	9.3	-2.8
2_1	92.2	35.4	79.9	10.7	-1.7
3	93.3	35.7	80.7	10.6	-2.1
4_0	92.4	35.6	80.5	9.4	-2.7
4_1	91.8	35.1	79.2	10.7	-2.1
5_0	299.9	123.7	279.2	9.7	-3.7
5_1	299.5	124.5	281.1	11	-2.5
6	299.4	124.4	280.9	10.8	-2.6
7	300	123.1	278	10.3	-3.9
8	218.7	89.7	202.5	10.5	-2.6
9_0	55.0	19.7	44.5	9.2	-2.4
9_1	54.6	18.9	42.8	10.2	-2.9

Table 5 – Estimate for each test of the pool energy balance by means of the performed measurements.

6.3 Water superheating

The analysis of the fluid temperatures measured above the heated rack confirms the presence of superheated water plumes that may in turn promote the occurence of the gravity-driven flashing underneath the liquid free surface. Indeed, by computing the difference between the mean fluid temperature above the rack and the saturation temperature (see Figure 9), the existence of superheated water can be highlighted for those tests with an overall heat power exceeding 90 kW. Generally, for those superheated plumes, the mean fluid temperature is higher than the saturation one by about 1/1.5°C (those values are greater than the measurement uncertainties and are hence significant, see Table 2). It follows that during the thermal saturation plateau, the liquid within the uprising plumes is prompt to yield some flashing through the form of bubbles. Consistently, for the test conducted at a power of 55 kW, neither any significant water superheating nor any flashing are observed. In Figure 9, it has also to be noted that the water superheating decreases during the transient, reflecting the evolution of the vaporization regimes that has been discussed in Section 6.1. For the tests conducted with a heterogeneous loading pattern such as LP3 (“hot spot”) and LP4 (“irregular”), for which the hottest cells are all concentrated in the same area of the rack, it is interesting to distinguish the temperature measurements performed on top of both the hot and cold regions of the rack, before computing a water superheating degree. In doing so, three temperature differences, denoted as DT1, DT2 and DT3, can be envisioned. Those quantities are computed as follows:

- DT1 = Mean temperature from temperature measurements of all multipoint sensors in the basin - Saturation temperature;
- DT2 = Mean temperature from temperature measurements of multipoint sensors above the hot cells - Saturation temperature;
- DT3 = Mean temperature from temperature measurements of multipoint sensors above the cold cells - Saturation temperature.

The obtained results, given in Table 6, show that the computed water superheating degrees are significantly different (up to 1°C) depending on the considered area of the differentially heated rack with the loading pattern LP3 (“hot spot”). However, this is not observed for the test conducted with the loading pattern LP4 (“irregular”), for which no significant difference appears.

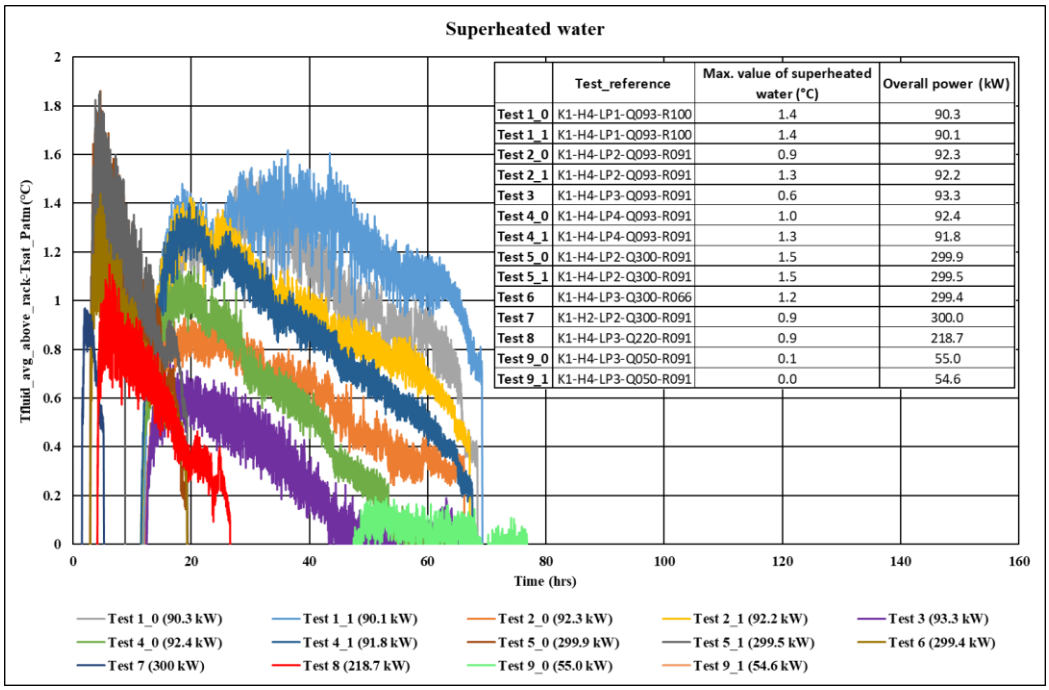

Figure 9: The computed water superheating degrees for all tests.

Test	Loading pattern	Max. value of water superheating (°C)		
		DT1	DT2	DT3
3	LP3	0.6	1.0	0.5
4_0	LP4	1.0	1.0	1.0
4_1	LP4	1.3	1.3	1.3
6	LP3	1.2	1.8	0.9
8	LP3	0.9	1.7	0.7

Table 6 – Obtained water superheating degrees for the tests conducted with a heterogeneous loading pattern.

6.4 Measured fluid temperatures

In Figure 10 to Figure 13 are given all the fluid temperature measurements, performed either at the rack outlet or within the liquid bulk, by means of the multipoint sensors (see Figure 4 to identify the heated cells within the rack on top of which those measurements are performed). In addition, the saturation temperature is also given. In the legend of these figures, the positions of the performed measurements are provided, with the position z = 1320 mm corresponding to the top of the rack. Reminding that the uncertainty of these measurements is equal to +/- 0.5 °C for temperatures of the order of 100 °C (see Table 2), it can be stated that for the "uniform", "regular" and "irregular" loading patterns, the temperature of the fluid above the rack is

spatially homogeneous by about +/- 0.5 °C, from 300 mm above the top of the rack. Only the fluid leaving the hot cells with a heating power of at least 4 kW is significantly warmer than elsewhere. For the “hot spot” loading pattern, the liquid on top of the area where the hottest cells are concentrated is significantly hotter than elsewhere. Moreover in this case, a visible temperature gradient of a few degrees, which depends on the heat power, suggests the existence of a thermal plume in between the top of the hot cells and the free surface. It is also to be noted that if the heat power of the cold cells is sufficient (this is the case for Test No. 6), the temperature of the fluid at the outlet of the rack is also, in average, significantly higher than elsewhere. Lastly, the noticeable fluid temperature fluctuations, which naturally depend on the heat power, are strong in the vicinity of the heat source and weaken when moving away from it, as seen in the below figures.

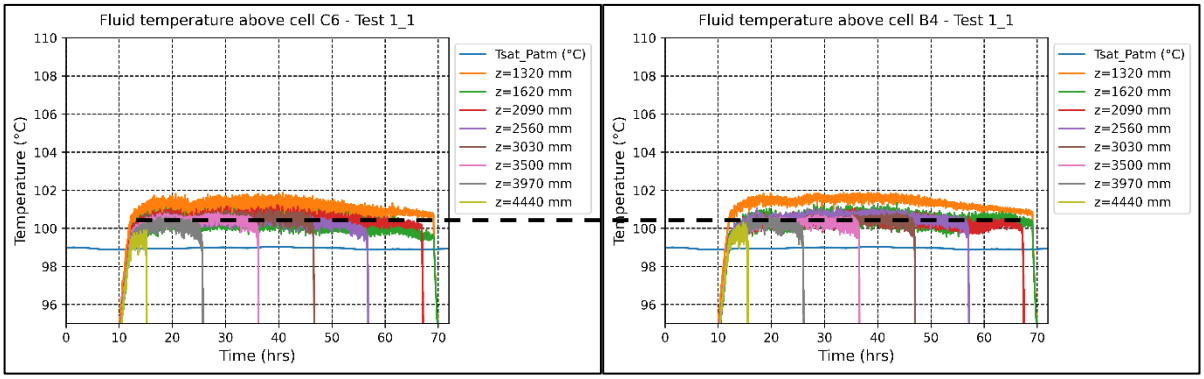

Figure 10: Temperature profiles above the heated cells – “uniform” loading pattern LP1.

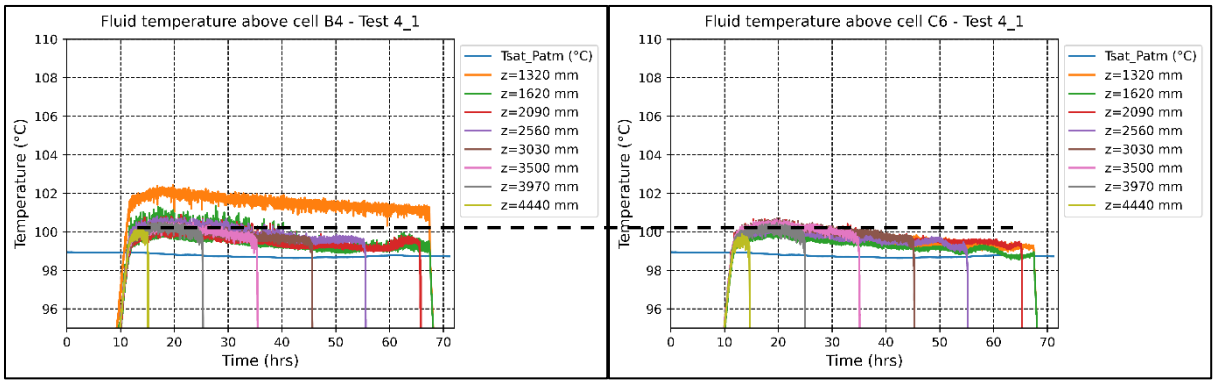

Figure 11: Temperature profiles above the heated cells – “irregular” loading pattern LP4.

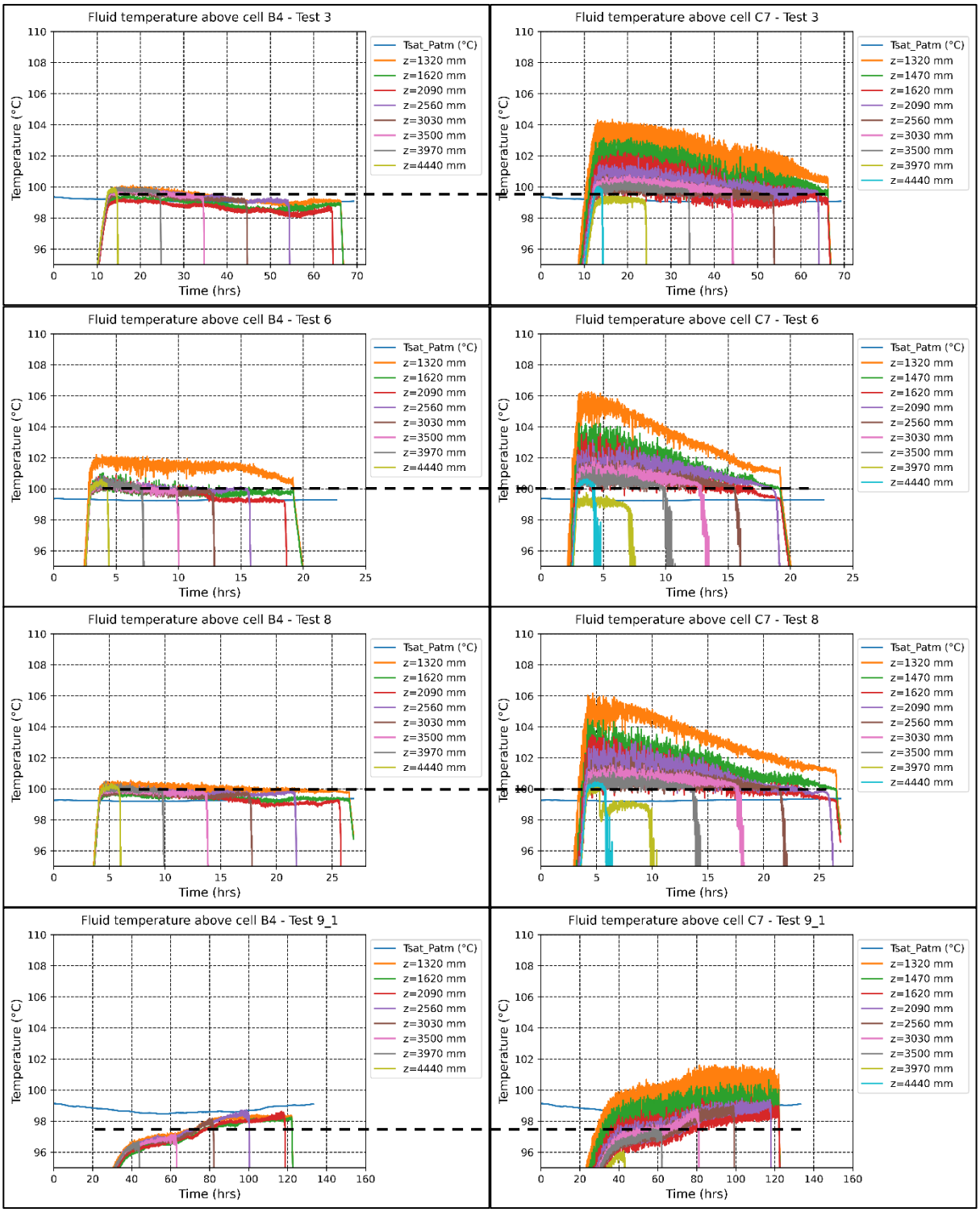

Figure 12: Temperature profiles above the heated cells – "hot spot" loading pattern LP3.

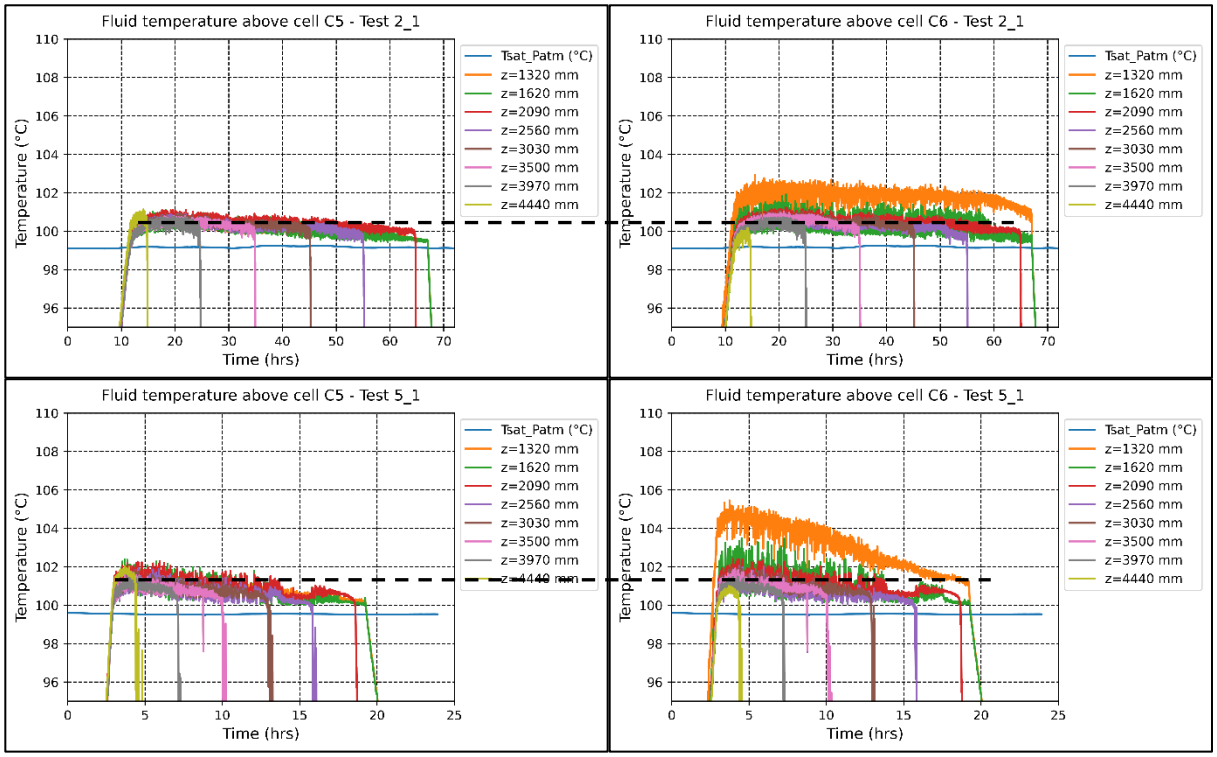

Figure 13: Temperature profiles above the heated cells – "regular" loading pattern LP2.

6.5 Flowrates in the heated cells

As exhibited in Figure 14, which gives simultaneously the flowrates measured in the heated cells of the rack and the collapsed water level during a transient at 300 kW and with the "regular" loading pattern, the flowrates are primarily controlled by the applied heat power, since two different types of trends appear: the first one relates to the hot cells having a heat power of 27.3 kW and the second is associated with the cold cells having a heat power of 2.4 kW. This result also shows that, in the MIDI facility, the head loss in the rack does not influence significantly the flowrates in the cells, since cells with an identical heat power but a different head loss (due to a different location in the rack) exhibit approximately the same flowrates. In addition, a close look at those flowrates highlights the different heat and mass transfer regimes reached within the pool. Those regimes, respectively denoted as A, B, C, D and depicted in Figure 14, are detailed in what follows:

- A – During that stage, there only exists a single-phase regime of heat and mass transfers within the pool, which corresponds to moderate mass flowrates within the cells;
- B – As soon as the two-phase flashing regime appears, the heated cells flowrates are substantially increased, presumably because of some large-scale liquid entrainment, induced by the bubbles appearing underneath the free surface;
- C – The water level is now low enough to promote the occurrence of nucleate boiling within the rack, which in turn increases significantly the heated cells flowrates;
- D – As soon as the heating power is off, all cells flowrates drop to a low level. During the cooling, residual flows that are identical for all cells, still exist, thereby highlighting some remaining thermal exchanges between the pool and its boundaries.

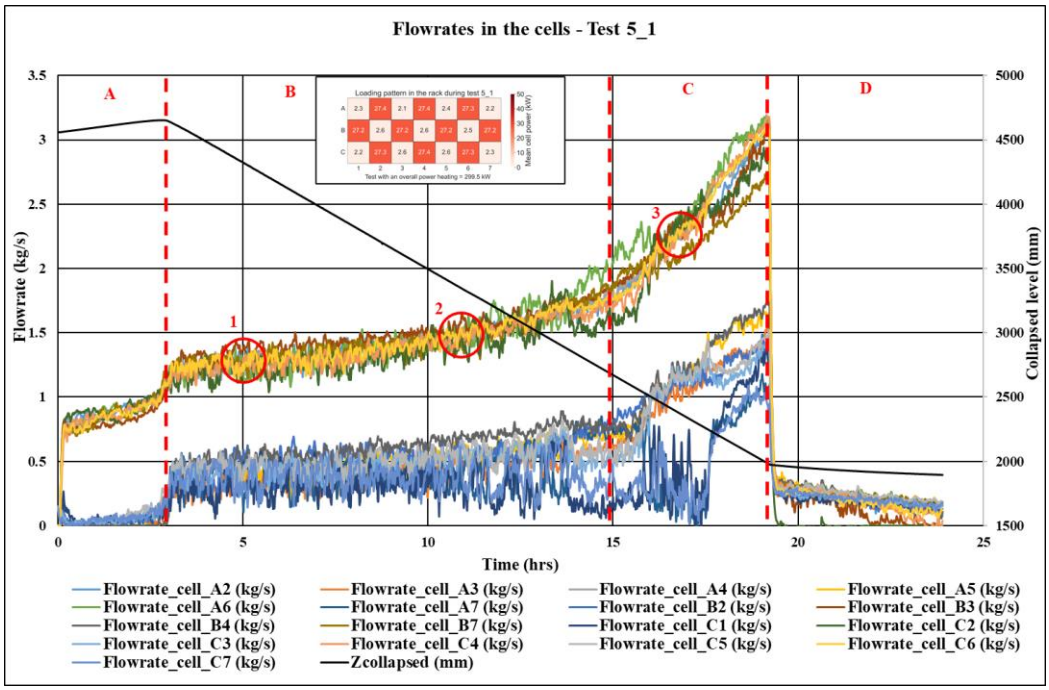

Figure 14: Time-trend of the measured heated cells flowrates during a test conducted at a power of 300 kW (Test 5_1).

This kind of analysis allows having a better understanding of the phenomena occurring during the simulated transient. In Figure 15, the flowrates that were measured during the other tests are given with the same presentation as for Figure 14. During all tests, the flowrates in the cold and hot cells are still different, except for test 1_1 which is the only one performed with a "uniform" loading pattern. As discussed earlier in this section, at the onset of flashing, a significant increase in the heated cells flowrates is always noted. Another jump in the cells flowrates is noted when some nucleate boiling initiates within the rack.

For those tests during which the nucleate boiling is significant, a preliminary characterization was performed in a specific facility to assess the area-averaged void fraction at the outlet of the cells (*cf.* Section **Erreur ! Source du renvoi introuvable.**). Table 7**Erreur ! Source du renvoi introuvable.** summarizes the void fraction values at the time corresponding to the circles depicted in Figure 14 andFigure **15**. As expected, the void fraction strongly depends on the water level, which imposes a local absolute pressure, and on the heat power. As shown in Table 7, the estimated void fractions remain moderate and lower than 5%, whatever the conducted test, with a water level which remains 1 m above the rack outlet section.

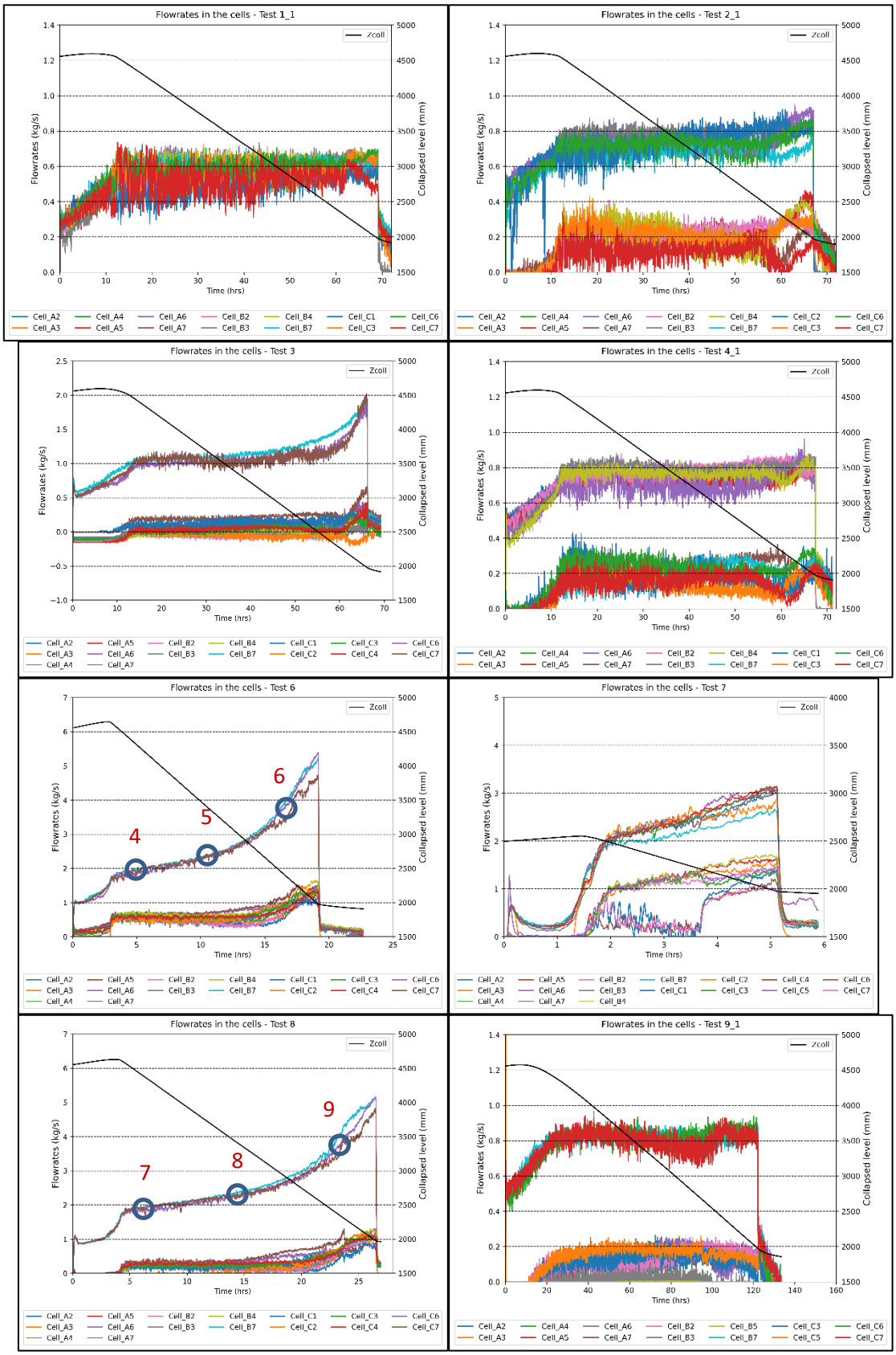

Figure 15: Individually measured flowrates in the heated cells, given for all tests.

Test	Circle ref.	Cell flowrate	Water level	Heating power	Inlet temperature of the rack	Void fraction (%)
5_1	1	~ 1.3 kg/s	~ 3 m above the rack	27.3 kW	100.5 °C	< 0.1 %
	2	~ 1.5 kg/s	~ 2 m above the rack		100.3 °C	< 0.1 %
	3	~ 2.3 kg/s	~ 1 m above the rack		100.1 °C	~ 1 %
6	4	~ 1.9 kg/s	~ 3 m above the rack	49.5 kW	100.1 °C	< 0.1 %
	5	~ 2.2 kg/s	~ 2 m above the rack		99.6 °C	~ 1 %
	6	~ 3.8 kg/s	~ 1 m above the rack		99.8 °C	~ 5 %
8	7	~ 1.9 kg/s	~ 3 m above the rack	50.0 kW	99.8 °C	< 0.1 %
	8	~ 2.2 kg/s	~ 2 m above the rack		99.6 °C	~ 1 %
	9	~ 3.8 kg/s	~ 1 m above the rack		99.8 °C	~ 5 %

Table 7 – Estimated void fractions at the rack outlet section.

6.6 Dissolved oxygen

During all tests, the measured O_2 concentration decreases from the very beginning. As long as the fluid temperatures remain below 80°C, the degassing remains moderate (*cf.* Figure 16). However, when these temperatures exceed 80°C, the O_2 concentration drops sharply and is almost equal to zero when the thermal saturation plateau is reached. It follows that the O_2 supersaturation (*i.e.* the difference between the measured O_2 mass concentration and the estimated O_2 solubility) increases at the beginning of the test, since the solubility decreases faster than what does the O_2 concentration. Then, the O_2 saturation decreases to be almost zero throughout the thermal saturation plateau. Ultimately, as soon as the heating system is shut down and the tests are stopped, the O_2 solubility increases again because of the water cooling, in a much faster fashion than the O_2 concentration.

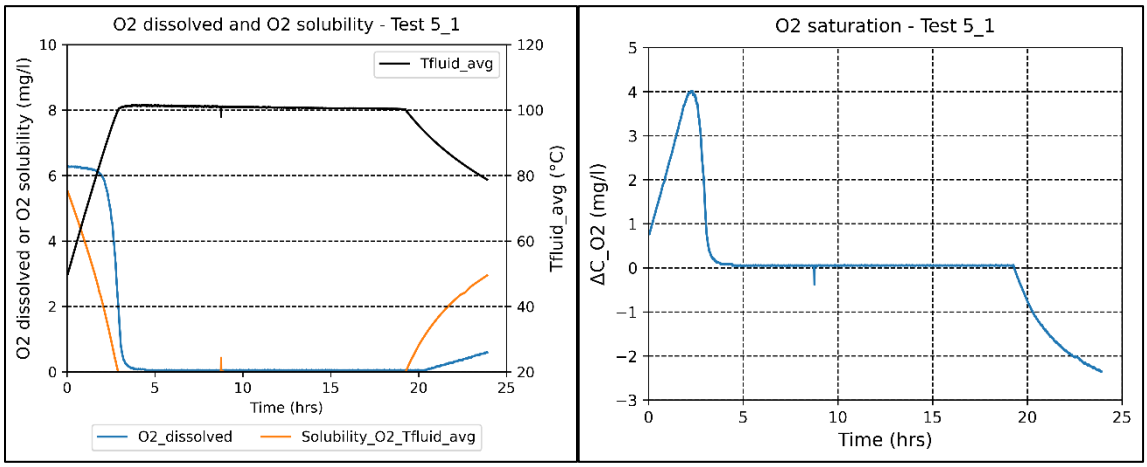

Figure 16: Time-trends of the measured dissolved oxygen concentration during all tests.

Overall, the O_2 concentration follows the above pattern for all tests, with however a different kinetics, as shown in Figure 17, where the O_2 concentrations are normalized by their initial value. At first glance, one can notice that those kinetics depend on the imposed heat power: the results associated with the tests conducted at 55 kW, 93 kW, 220 kW and 300 kW are clearly different. Test No.7, performed with a power of 300 kW, differs from

those tests having a similar power. Indeed, being started with a lower water level, the initial amount of dissolved O_2 is necessarily lower, which in turn obviously impacts the degassing kinetics.

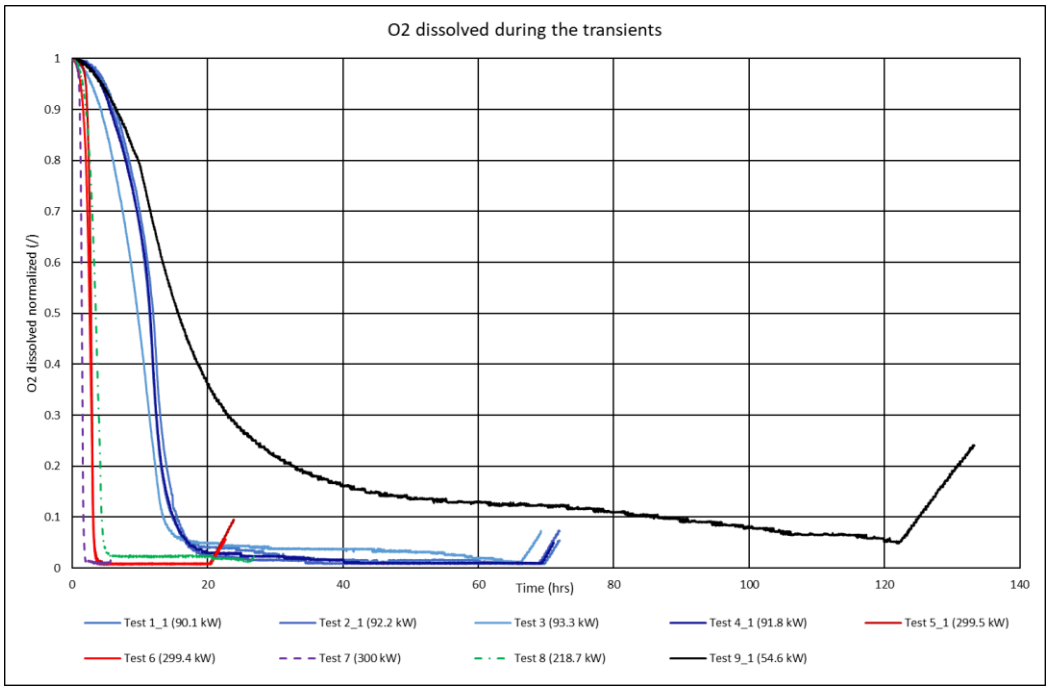

Figure 17: Normalized dissolved oxygen mass concentrations for all tests.

7. CONCLUSIONS AND PERSPECTIVES

A first experimental campaign was carried out in MIDI, a unique experimental tool which allows simulating at a laboratory scale the thermal hydraulics of a spent fuel pool undergoing a loss-of-cooling accident, before the stored fuel assemblies get uncovered. In the framework of the DENOPI project, nine tests were achieved and allowed investigating the phenomenology of this type of accident. As highlighted, this phenomenology is characterized by three competing liquid vaporization mechanisms: the evaporation at the pool free surface, the nucleate boiling within the fuel bundles and the gravity-driven flashing of superheated water on top of the storage racks. Pointedly, the existence of the latter vaporization mode, uncertain at the launch of the DENOPI project, is now confirmed in the configuration of a spent fuel pool, in agreement with earlier results published by IRSN in [4] and [9]. It is also to be noted that the contribution of the nucleate boiling becomes significant only when the pool water level is low enough and around 1 m above the heat source in the MIDI facility. Among the simulated loading patterns, only the ”hot spot” one yields significant differences in the void fraction distribution and temperatures within the pool upper volume. In this very case, the flashing phenomenon appears preferentially on top of the hot spot. For the other three tested loading patterns, the liquid temperature field appears quite homogeneous, except at the outlet section of the heated cells.

As a perspective, a first physical interpretation of the MIDI tests that were conducted up to date will be provided in a second part of the present article, available in [8]. This interpretation will include a first-level phenomenological analysis, the quantification of the envisioned modes of water vaporization, the construction of a so-called vaporization regimes map which allows predicting the most likely dominant vaporization mode, given the pool level and total heat power, and a set of dimensionless correlations for estimating the heat and mass transfers within the liquid pool.

8. ACKNOWLEDGMENTS

The DENOPI project was part of the "Investment for the future" program funded by the French Government within the framework of the post-Fukushima surveys, identified as major safety issues (contract number ANR 11 - RSNR 006). The French Government and the National Research Agency are gratefully acknowledged for their interest and financial support. Besides, IRSN thanks its project partners, US-NRC, Bel-V and EDF, for their valuable contributions.

9. REFERENCES

[1] OECD/NEA (2014). "Status Report on Spent Fuel Pools under Loss-of-Cooling and Loss-of-Coolant Accident Conditions – Final Report", Technical Report NEA/CSNI/R(2015)/2

[2] OECD/NEA (2018). "Phenomena Identification and Ranking Table: R&D Priorities for Loss-of-Cooling and Loss-of-Coolant Accidents in Spent Nuclear Fuel Pools", Technical Report NEA/CSNI/R(2017)/18

[3] J. Martin and N. Trégourès (2023). "OECD/NEA R&D priorities for loss-of-cooling and loss-of-coolant accidents in Spent-Fuel-Pools", Nuclear Engineering and Design, Vol. 410, pp. 112380

[4] J. Martin, P. Ruyer, M. Duponcheel and Y. Bartosiewicz (2023). "A novel experimental observation of the gravity-driven flashing of metastable water in a heated pool", Nuclear Engineering and Design, Vol. 410, pp. 112371

[5] F. Yan and M. Giot (1989). "Mechanisms of nucleation in flashing flows", in Proc. 7th EUROTHERM Seminar, Thermal Non-Equilibrium in Two-Phase Flow, Roma, Italy, March 23-24, 1989

[6] A. Bousbia-Salah and J. Vlassenbroeck (2012). "Survey of some safety issues related to some specific phenomena under natural circulation flow conditions", in Proc. EUROSAFE 2012, November 5-6, 2012, Brussels, Belgium

[7] R. B. Duffey, U. Rohatgi and E. D. Hughes. (1993). "Two-phase flow instability and dryout in parallel channels in natural circulation", in Proc. National Conference and Exposition on Heat Transfer, August 8-11, 1993, Atlanta, Georgia, USA

[8] J. Martin and B. Migot (2024). "An experimental study of the thermal-hydraulics of a spent nuclear fuel pool under loss-of-cooling accident conditions. Part II: a first interpretation of the MIDI tests", Nuclear Engineering and Design, *on press*

[9] J. Martin (2023). "The gravity-driven flashing of metastable water in a pool heated from below – An experimental study", PhD thesis, Université Catholique de Louvain, Institute of Mechanics, Materials and Civil Engineering, Louvain-la-Neuve, Belgium

[10] J. H. Lienhard IV and, J. H. Lienhard V (2008). "A heat transfer textbook", Third edition, Phlogiston press, Cambridge, Massachusetts

[11] R. Krishnamurti (1970). "On the transition to turbulent convection", Journal of Fluid Mechanics, Vol. 42, pp. 295

[12] C. Tompkins, H.-M. Prasser and M. Corradini (2018). "Wire-mesh sensors : a review of methods and uncertainty in multiphase flow relative to other measurement techniques", Nuclear Engineering and Design, Vol. 337, pp. 205-220

[13] T. C. Hung, V. K. Dhir, B.-S. Pei, Y.-S. Chen and F. P. Tsai (2013). "The development of a three-dimensional transient CFD model for predicting cooling ability of spent fuel pools", Applied Thermal Engineering, Vol. 50, pp. 496-504

[14] J. Martin, T. Kamin and P. Ruyer (2017). "Analysis of the Fukushima-Daiichi Unit-4 Spent Fuel Pool loss-of-cooling accident by means of the TETHYS code: highlight of major thermal-hydraulic modeling issues", in Proc. 17th NURETH conference, Xi'an, China, September 3-8, 2017

[15] A. Lu. (2002). "A review of geysering flows", in Proc. 24th NZ Geothermal Workshop, 2002, Auckland, New Zealand